Plasma Research Express

Influence of magnetic field strength on nanoparticle growth in a capacitively-coupled radio-frequency Ar/C_2H_2 discharge

Plasma Research Express

OPEN ACCESS

RECEIVED
12 October 2018

REVISED
21 January 2019

ACCEPTED FOR PUBLICATION
4 February 2019

PUBLISHED
12 February 2019

PAPER

Influence of magnetic field strength on nanoparticle growth in a capacitively-coupled radio-frequency Ar/C_2H_2 discharge

L Couëdel[1,2,3], D Artis[3], M P Khanal[3], C Pardanaud[2], S Coussan[2], S LeBlanc[3], T Hall[3], E Thomas Jr[3], U Konopka[3], M Park[3] and C Arnas[2]

[1] Department of Physics and Engineering Physics, University of Saskatchewan, Saskatoon, Saskatchewan S7N 5E2, Canada
[2] CNRS, Aix Marseille Univ., PIIM, UMR 7345, 13397 Marseille cedex 20, France
[3] Department of Physics, Auburn University, Auburn, Alabama 36849, United States of America

E-mail: lenaic.couedel@usask.ca **and** lenaic.couedel@univ-amu.fr

Keywords: plasma, nanoparticles, magnetic field

Abstract

The growth of nanoparticles in a magnetised chemically active discharge (Ar/C_2H_2) is investigated. The influence of the strength of the magnetic field on dust particle growth dynamics is explored. The structure of the grown nanoparticles is studied *ex situ*. It is revealed that the strength of the magnetic field (up to 2.5 T) has a major impact on discharge parameters (such as the self-bias of the powered electrode) as well as on the growth and morphology of the nanoparticles. At high magnetic field, the dust cloud is confined in the sheath above the grounded electrode while without magnetic field the dust cloud occupies most of the interelectrode space. Moreover, at high magnetic field, large porous spherical agglomerates were grown. The modification of the self-bias is explained by the influence of the magnetic field on the diffusion of charged species resulting in a confinement of the plasma under the powered electrode. Complementary particle-in-cell simulations confirm that the electric field and plasma distributions are strongly affected by the magnetic field explaining the experimentally observed dust cloud localisation. The large porous spherical agglomerates are most probably due to an enhanced agglomeration caused by the modified confinement owing to the magnetic field.

1. Introduction

Dusty or complex plasmas are weakly ionised gases containing nanometre or micron size dust particles. In laboratory plasmas, due to their interactions with the background electrons and ions, these dust particles are electrically charged. This charge is usually negative due to the higher mobility of the electrons. Complex plasmas can thus be viewed as three charged component plasmas [1–3].

In nature, dusty plasmas can occur naturally in the mesosphere, interplanetary and interstellar clouds, planetary rings [4, 5], and cometary tails. In these systems the dust particles are formed from the agglomeration of complex molecules and ices that occur in the space environment [6]. Dust particle formation is also observed in the laboratory (see for example [7–9]) and industrial [10] chemically active discharges. Dust particle formation in an industrial reactor is an important issue: the occurrence of solid dust particles (nano- or micrometric) is unwanted (and even harmful) in some processes such as etching as it significantly changes the electrical properties of the discharge. As a result, the presence of growing dust particles can substantially alter the plasma etching processes and lead to substrate pollution. However, the dust particles can also be of value for technologies based on nanomaterials and nanocomposites, such as polymorphous silicon (amorphous silicon with embedded crystalline silicon nanoparticles created in silane-based discharges), a material of primary interest for the manufacture of solar cells [11]. Low-pressure radiofrequency plasmas have been thus extensively used in 'dusty-regime' as a tool to produce high quality nanocrystals and nanopowders of a broad range of materials [12]. The understanding of dust growth mechanisms in plasmas is consequently a crucial issue and is of interest to many subfields of plasma physics.

In capacitively-coupled radio-frequency (cc-rf) discharges, dust growth mechanisms have been actively studied. Dust growth occurs following a well-defined pattern: formation of molecular precursors from sputtering products or by gas dissociation, formation and accumulation of nanocrystallites, aggregation and finally growth by molecular sticking [8, 11, 13, 14]. Particle growth depends on the discharge parameters [12] and the dust growth has a significant impact on the surrounding plasma [15, 16]. It is thus imperative to monitor the evolution of the discharge and plasma parameters carefully to have a full understanding of the growth process.

In the presence of a magnetic field, the transport of electrons and ions is altered and thus the properties of the plasma are affected. In a dusty plasma under low to moderate magnetic fields (or for large enough dust particles) the influence of the magnetic field is indirect and weak, due to the very small charge-to-mass ratio [17]. However, even at these low magnetic fields ($B < 1$ T) dust grain surface electron and ion fluxes will experience modifications. As a result, the dust particle charges and the forces acting on them are changed and the drag forces resulting from these ion and electron flows are of great importance for the dynamics of dust particles.

In moderately magnetised conventional discharges, dust particle growth is observed [18–20]. In such discharges, the magnetic field is used to trap electrons and thus enhance the plasma density through an increase in the number of ionising collisions. For example, in magnetron sputtering discharges, it is possible to grow and trap a dense cloud of metallic nanoparticles above the cathode [19]. In magnetron discharges, dust rotation arising from the ion $\mathbf{E} \times \mathbf{B}$ drift is sometimes observed and can be used to enhance particle coating [21]. In electron cyclotron resonance (ECR) discharges, the growth of nanoparticles occurs in the high magnetic field regions [20]. This means that the electrons trapped in this region (Lorenz force must be considered for electrons dynamics and transport) create plasma potential wells able to confine the negatively charged dust particles. Dust particle growth can be monitored by measuring the self-bias voltage of a probe immersed in the ECR plasma.

In this paper, we report on measurements of the plasma and characterisation of nanometre-sized particles that were formed in magnetised plasmas. Experiments were performed using the Magnetized Dusty Plasma Experiment (MDPX) device using a modified rf plasma source. Plasmas were generated in pure argon (Ar) or in a mixture of argon and acetylene (C_2H_2) gas. The magnetic field was varied from 0 T to 2.5 T. This paper reports on changes in discharge parameters such as the self-bias of the powered electrode due to the magnetic field in pristine argon discharge as well as the effect of dust particle growth in magnetised argon-acetylene discharges. It also reports on the characterisation of the grown particles using electron microscopy and Raman spectroscopy. The paper is presented as follows: section 2 describes the experimental set-up, section 3 describes the characterisation of the plasma discharge, section 4 describes the characterisation of the particles, section 5 presents a numerical model of the system and particle-in-cell simulations in order to qualitatively explain our results. Finally, section 6 will provide concluding remarks.

2. Experimental setup

The Magnetized Dusty Plasma Experiment (MDPX) device at Auburn University is a multi-user, high magnetic field experimental platform. It consists of two main components: the superconducting magnets and a plasma chamber which can be changed according to the type of experiments. The superconducting magnets of the MDPX device are described extensively in previous papers [17, 22, 23]. For the studies reported in this article, the MDPX device was operated in the vertical configuration (magnetic field aligned parallel to gravity). The four superconducting coils were energised at the same current to produce a uniform magnetic field (with $\Delta B/B < 1\%$) at the center of the experimental volume where the cc-rf discharge was placed.

The plasma source consisted of parallel aluminium electrodes installed at the center of a 6-way cross vacuum chamber with 100 mm ISO ports (see figure 1). A 13.56 MHz rf generator connected to the powered electrode through a matching network was used to produce the plasma. The rf power was set between $5 < P_{rf} < 30$ W. The top electrode with a diameter of 50.8 mm was powered and surrounded by a grounded guard ring. The powered electrode developed a self-bias, V_{bias} when the plasma was on, which was monitored using a National Instrument data acquisition card. The grounded bottom electrode had a diameter of 76.2 mm and a ~1 mm deep, 25 mm wide 75 mm long notch was cut in its center in order to install the microscopy glass slides used to collect the grown particles.

Before each plasma the vacuum chamber was evacuated to a base pressure of ~1 mTorr. Then a flow of argon $5 < Q_{Ar} < 10$ sccm and a flow of acetylene $0 < Q_{C_2H_2} < 2$ sccm were injected into the chamber and the opening of the pumping port was adjusted to stabilise the pressure p inside the chamber to a value 200 mTorr $< p <$ 600 mTorr before the plasma was switched on. The pressure was monitored using a MKS Baratron capacitance manometer. The grown particle cloud was then illuminated using a 532 nm, 100 mW green laser diode that was expanded into a thin, vertical laser light sheet (~3 cm height, ~200 μm width) using a cylindrical lens. The scattered light was recorded from the side port of the vacuum chamber at an angle of 90°

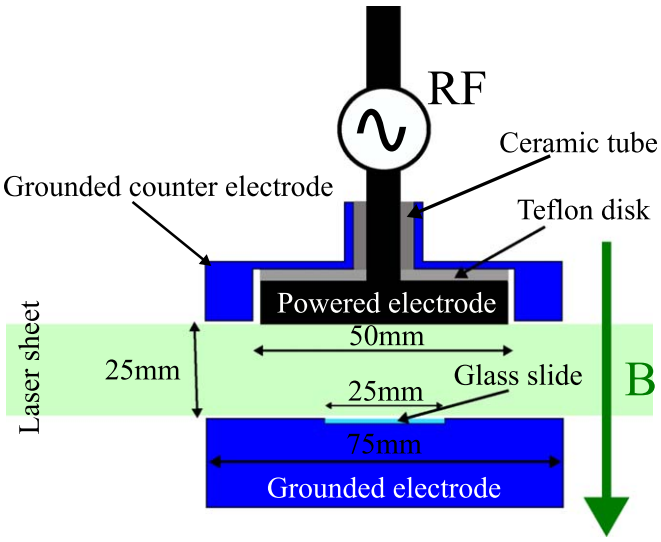

Figure 1. Schematic of the electrode assembly.

using a USB3-based, 2048 by 2048 pixel, Ximea model xiQ camera that could be operated up to 90 frames per second (fps). For the experiments described in this article, frame rates of 30 fps were usually used.

3. Discharge characterisation

3.1. Pristine argon plasma

The behaviour of the discharge as a function of the magnetic field strength was studied in pristine argon (experiments with no particle growth). The operating pressure was $p = 300$ mTorr ($Q_{Ar} = 7$ sccm) and the forward rf power $P_{rf} = 20$ W. A clean glass slide was installed in the notch of the bottom grounded electrode. The magnetic field was set at an initial high value of 2.5 T and was then slowly ramped down to 0.0 T. The plasma glow was recorded at 1 fps and the self-bias voltage of the powered electrode was measured. In figure 2, snapshots of the plasma glow for different magnetic field strengths are presented. As can be seen, the plasma light emission appears to increase with the magnetic field . Moreover, the glow is generally more localised under the powered electrode at high magnetic field, indicating a strong confinement of the charged species. Note that with magnetic fields $B > 0.25$ T, filamentation of the plasma occurred. Filaments were mostly localised at the edge of the powered electrode. The number of observed filaments was higher for the highest values of magnetic field. Note that the filaments were not fixed and could jump from one position to another. It is unclear what role these filaments could play in the subsequent growth experiments in which they were also observed.

In figure 3, the evolution of the self-bias voltage as a function of magnetic field strength is presented. As expected, at low magnetic field the self-bias is negative because the surface of the powered electrode is smaller than the surface of the grounded areas [24, 25]. When increasing the magnetic field, the self-bias of the powered electrode increased (or decreased in absolute value) and reached 0 V at B~1 T. At magnetic field $B \gtrsim 1$ T, the self-bias started to decrease again. Note that the magnetic field did not noticeably affect the settings of the matching network and therefore the impedance of the whole circuit (plasma + external circuit) was almost constant. Consequently, the variations of rf peak to peak voltage at the powered electrode remained limited and could not explain the amplitude of the changes of the self-bias voltage. The physical mechanism of the self-bias evolution as a function of the magnetic field strength are discussed in section 5.1.

3.2. Ar/C_2H_2 discharge

When adding acetylene to the discharge, carbon nanoparticles could be grown. During our experiments, the pressure was set to $p = 300 \pm 2$ mTorr before plasma ignition using an Ar/C_2H_2 gas mixture ($Q_{Ar} = 7$ sccm and $Q_{C_2H_2} = 1$ sccm). The forward rf power was $P_{rf} = 20$ W. The discharge was pulsed manually with plasma duration $t_{on} = 60$ s followed by pauses of $t_{off} \simeq 60$ s. In figure 4(a) the evolution of the pressure normalised to the maximum pressure during the plasma pulse is presented. As can be seen, after the discharge was turned on, the pressure slightly increased to a maximum p_{max} due to heating of the gas. However, after 1 s, the total gas pressure started to decrease. The value at the end of the plasma pulse was 3%–4% lower than the pressure at ignition (well below the experimental pressure fluctuations due to our gas flow regulation system). This indicates that, while the acetylene flow was kept constant, it was partially dissociated. This behaviour was observed for all

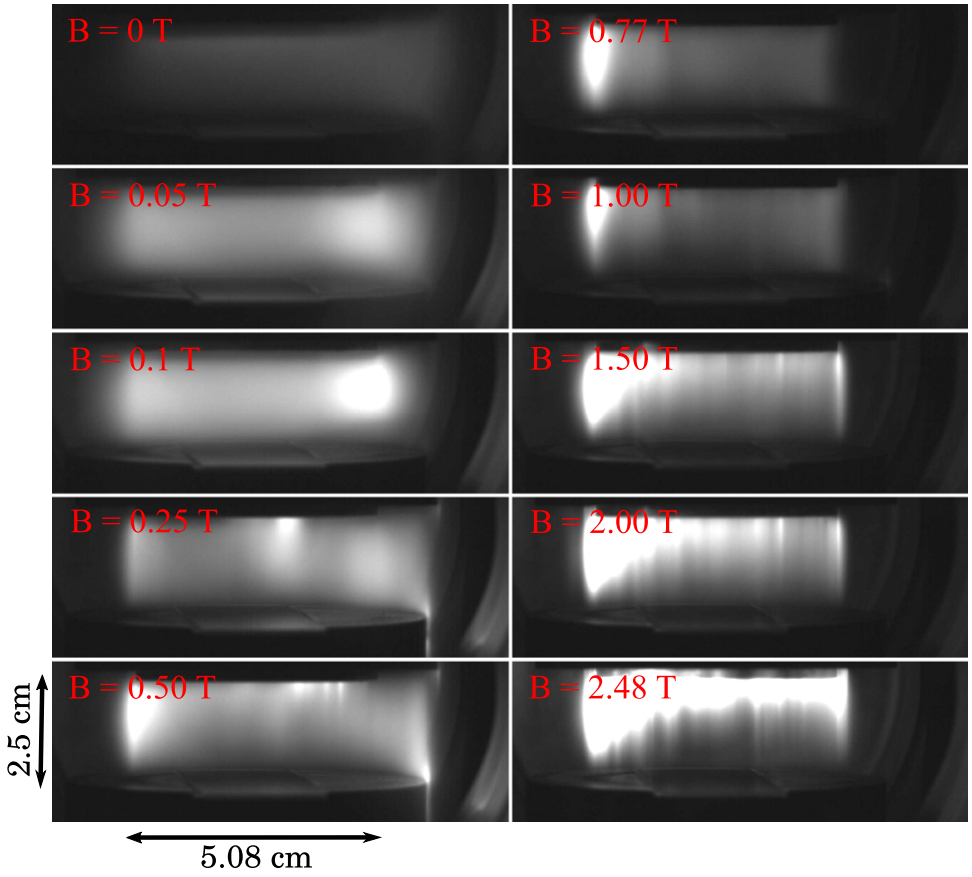

Figure 2. Snaphots of the plasma glow at different magnetic fields for pure argon plasmas. The argon flow was $Q_{Ar} = 7$ sccm, the pressure was $p = 300$ mTorr and the rf power was $P_w = 20$ W.

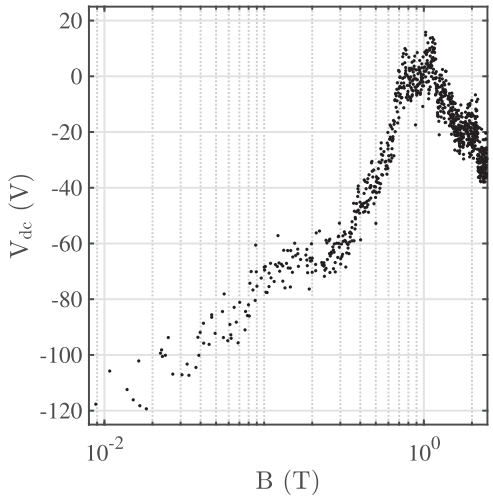

Figure 3. Self-bias as a function of magnetic field strength. Discharge parameters are the same as in figure 2.

magnetic fields. It should be nevertheless noted that increasing the magnetic field resulted in a faster and greater decrease of the pressure (the pressure decay rate is faster in the presence of a magnetic field and the minimum reached pressure is the smallest for the largest value of the magnetic field). In all cases at the end of each rf pulse, the pressure returned to its original value in ~30 s.

The self-bias voltage of the powered electrode V_{bias} was also recorded during the different discharge pulses. The results are presented in figure 4(b) for different magnetic field strengths. The general behaviour observed in pure argon plasma was again observed, i.e. the stronger the magnetic field, the lower (in absolute value) the self-bias. However, contrary to pure argon plasma, the self-bias was not constant with time. It is known that the

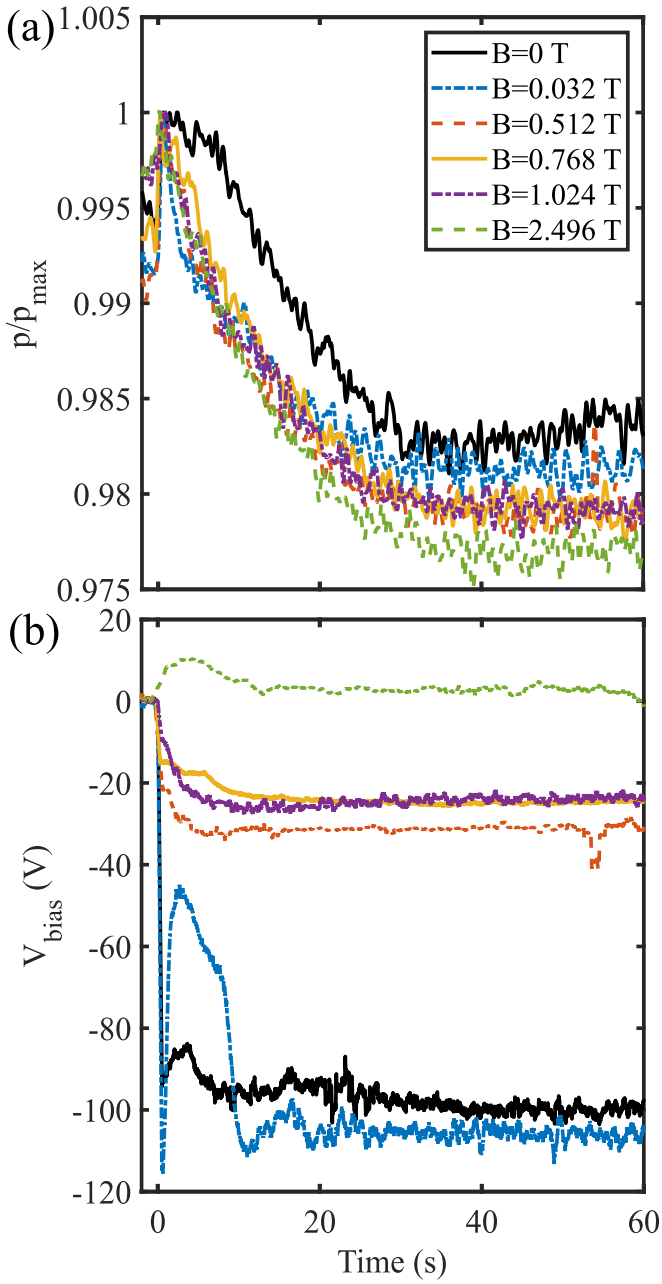

Figure 4. Evolution of (a) normalised chamber pressure and (b) self-bias voltage as a function of time for different magnetic field strengths in Ar/C_2H_2 discharges. The argon flow was $Q_{Ar} = 7$ sccm, the acetylene flow was $Q_{C_2H_2} = 1$ sccm, the pressure before ignition was $p = 300$ mTorr and the rf power was $P_w = 20$ W.

growing nanoparticles strongly affect the impedance of the plasma (see for examples [26]) and that working at fixed rf power therefore induces variations of the rf peak to peak voltage. These variations are correlated to the variations the self-bias voltage and directly associated to the growth dynamics of the nanoparticles. Large self-bias oscillations are linked to successive generation of nanoparticles as was already reported in cc-rf discharge in which particles are grown [7, 27–30]. However, at low or zero magnetic field, V_{bias} exhibited strong oscillations in the first 20 s after plasma ignition. The strongest oscillations were observed at $B = 0.032$ T (see figure 4(b)). Note that from one plasma to the other the shape of the V_{bias} signal was roughly the same (slight changes due the change in discharge conditions, i.e. coating of the electrode, gas purity, temperature of the electrode, etc). It should also be noted that at the highest investigated magnetic field ($B = 2.496$T), the self-bias of the powered electrode was, contrary to the pristine argon discharge, positive. In an electropositive plasma (such as a pristine argon plasma), the main reason for the appearance of self-bias on the powered electrode connected to the rf generator through a blocking capacitor (as in many rf matching network) is the irreversible escape of electrons into the electrodes, making the gap positively charged [24]. Since the discharge is asymmetric (the grounded area are much bigger than the area of the powered electrode), different amounts of charge are gained by the

electrodes. It causes a difference in the dc electrode potentials, the self-bias. In Ar/C_2H_2 discharges in which particles are growing, there are numerous kind of charged species (positive and negative ions such as Ar^+, $C_2H_2^+$, C_2H^-, $C_4H_2^+$, etc) due to the complicated chemistry [31–34]. Moreover, the growing dust particles are getting negatively charged which reduces the electron density [35].Consequently, the observed positive self bias is most probably caused by a very different balance of the charges collected at the electrodes due to the complicated chemistry of the Ar/C_2H_2 plasma and the presence of the growing particles.

In figure 5, snapshots of the laser light sheet scattered by the growing particle cloud at different magnetic fields are presented. At no magnetic field (figure 5(a)) the well-known cyclic growth behaviour was observed: ∼15 s after plasma ignition, the dust cloud started to be visible on the camera and occupied almost the entire interelectrode space. At $t \sim 20$ s, a 'void' (i.e. a region without visible dust particles) started to open in the discharge (see figure 5(a) at $t = 20$ s in the middle of the gap below the powered electrode edge) [36–47]. Note that in our experiment, the void did not have its typical eye shape as reported by other groups. The observed void was more bowl-shaped. This is most likely due to the geometry of our experiment which differs from the ones used in other studies (size of the electrodes and/or interelectrode spacing). Inside the void opening new particles are growing while the first cloud was pushed towards the edges(see figure 5(a)). With our experimental parameters, the duration of a growth cycle (appearance of a new generation of dust in the 'void') was ∼40–60 s, depending on how many plasma pulses had already occurred in the chamber. Density waves were visible near the lower electrode. Such density waves were observed in similar experiments [48, 49] and are known to favour the agglomeration of the nanoparticles [48, 50].

At low magnetic field ($B = 0.032$ T, figure 5(b)) the nanoparticle growth was faster which was demonstrated by direct imaging of the nanoparticle cloud. This correlates well with the faster decrease of the gas pressure during the plasma pulses and the stronger oscillations of the self-bias voltage previously described. The duration of a growth cycle was, in this case, ∼15–20 s. An interesting observation is the break of symmetry in the void opening (see figure 5(b) at $t = 20$ s). Moreover, a strong scattering intensity was observed close to the sheath of the top electrode indicating a very dense particle cloud and/or the presence of large particles.

At higher magnetic field ($B \gtrsim 0.1$ T), no growth cycles were observed. In figure 5(c), snapshots of the recorded laser light scattering at $B = 1.024$ T are presented but qualitatively similar observations were made at other values of magnetic field. In all high magnetic field cases, a cloud of nanoparticles above the grounded bottom electrode rapidly appeared (see figure 5(c)). This is in agreement with the fast decrease of the gas pressure after plasma ignition due to the dissociation/polymerisation of acetylene resulting in the formation of the dust particles. It is interesting to note that the dust cloud did not cover the entire area above the grounded electrode but was on the contrary confined near the interface between the glass slide used for dust collection and the rest of the electrode. Depending on the experiment, the dust cloud extended more or less above the glass slide. Laser light scattering also confirmed a quick agglomeration. Large individual particles levitating above the grounded electrode were indeed visible on camera only a few tens of seconds after plasma ignition (see figure 5(b) at $t = 40$ s and $t = 60$ s). The particles formed much closer to the electrode compared to the cases at no and low magnetic fields.

4. Dust characterisation

For the different magnetic fields, dust particles were collected for fifteen consecutive 60 s plasma pulses separated by an off period of 60 s during which the gas was renewed. After each series of fifteen plasmas, the electrodes were carefully cleaned and a new glass slide was installed in the grooved bottom electrode. An argon oxygen plasma was then run in the chamber for ∼15 min at 20 W in order to burn away all residual carbon coating. Finally the chamber was pumped down to its base pressure for a minimum of 30 min before the next series of plasmas was performed.

4.1. Electron microscopy

In figures 6 and 7, scanning electron microscopy (SEM) images and transmission electron microscocopy (TEM) images of dust particles grown at different magnetic fields are presented. As can be seen in figures 6(a) and 7(a), the nanoparticles grown at $B = 0$ T were almost spherical and looked quite compact as reported in similar experiments [51]. The observed particles had diameters ranging from ∼20 nm to ∼250 nm in agreement with the observation of a couple of growth cycles during a 60 s plasma pulses. In the zoom of figure 7(a), the surface roughness of the nanoparticles seems to indicate that the nanoparticles are agglomerate of smaller particles as reported in similar experiments [51, 52].

Increasing the magnetic field greatly affected the shape and size of the nanoparticles. At low magnetic field (see figure 6(b)), the size distribution seemed much broader than without magnetic field but the particles still looked quite compact. This observation coincides with the faster growth cycle reported in section 3.2. A further

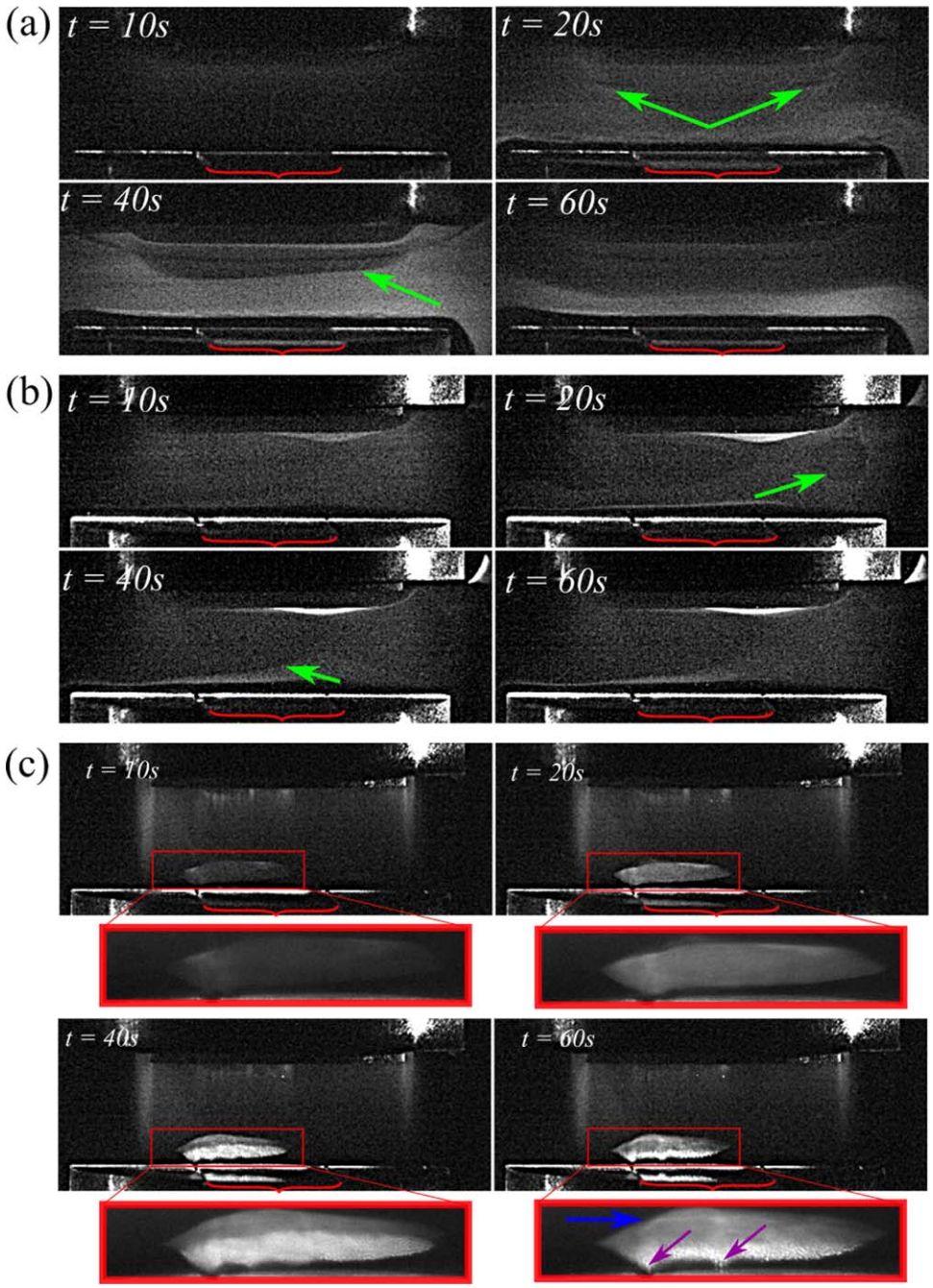

Figure 5. (a) Images of the scattered laser light at different instants after discharge ignition for: (a) B = 0.0 T, (b) B = 0.032 T and, (c) B = 1.024 T. The other discharge conditions are the same as in figure 4. The bright vertical and horizontal stripes visible on all images are reflections of the laser light on the electrode assembly. On all images, a red horizontal curly bracket indicates the position of the glass slide used to collect the dust particles. In (a) and (b), the oblique green arrows indicate the edge of the void in which a new generation of dust particles can grow. In (c), the horizontal blue arrow point to a dust density wave and the oblique purple arrows show dips in the dust cloud induced by plasma filamentation. On all images except the magnified ones, a sharpen filter has been applied to improve visibility of the different features.

increase of the magnetic field resulted in the sample being a mixture of very small (~10 nm) nanoparticles with larger spherical 'fluffy' porous particles (with diameters up to a few hundreds of nanometres). These particles are clearly visible in figures 6(c)–(d). TEM images (figures 7(b)–(d)) clearly show that these porous particles are agglomerates of the smaller particles. Both SEM and TEM images indicate that higher magnetic field resulted in fluffier agglomerates. The agglomerates are probably the large particles levitating in the sheath above the grounded electrode observed by laser light scattering in figure 5(c) towards the end of the plasma pulse. The smaller particles correspond to the dim cloud levitating slightly above the larger dust particles.

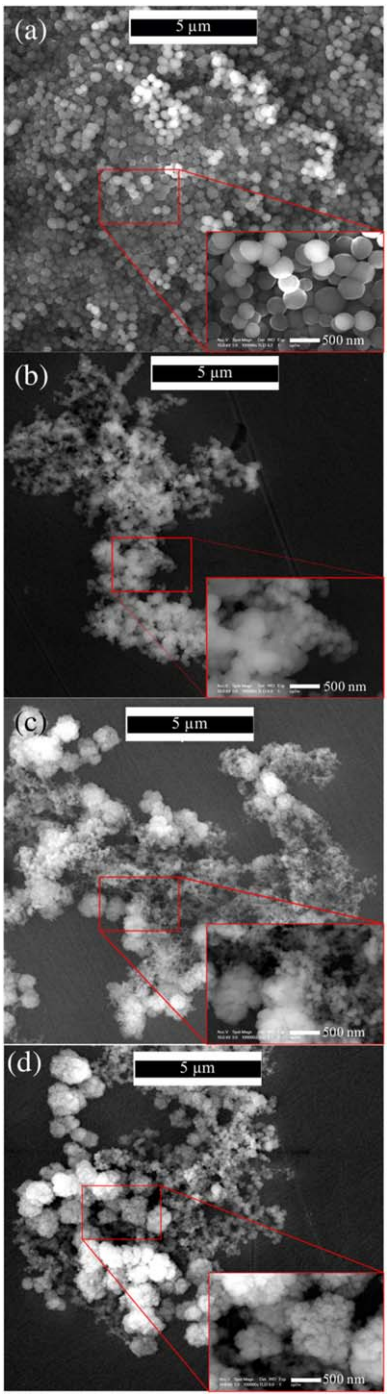

Figure 6. SEM images of dust particles grown for different magnetic fields. (a) 0 T, (b) 0.768 T, (c) 1.024 T and, (d) 2.496 T. The other discharge conditions are the same as in figure 4.

4.2. Raman microscopy

Carbon-based materials are routinely analysed using micro-Raman spectroscopy [53–61]. This technique consists in measuring the wavelengths of photons produced by inelastic scattering of the incident light with the analysed sample. The energy difference between incident and scattered photons correspond to vibrational energies which are fingerprints of a given material. Interpreting the spectral region between 1000 and 1800 cm^{-1} provides information on the chemical properties (hybridisation of the carbon atoms) and the structural order [53, 55, 60].

The Raman spectra were obtained using a commercial Horiba-Jobin-Yvon HR LabRAM apparatus ($\times 100$ lens, 514.5 nm, numerical aperture 0.9, laser power at the surface $\lesssim 1$ mW $\cdot$ μm^{-2}). The resolution of our system is ~ 0.2 cm^{-1}. Each final spectrum was an average of 9 spectra taken a few micrometers apart to avoid local inhomogeneity. The scanning time was ~ 60 s averaged two times. Spectra have been acquired at the centre

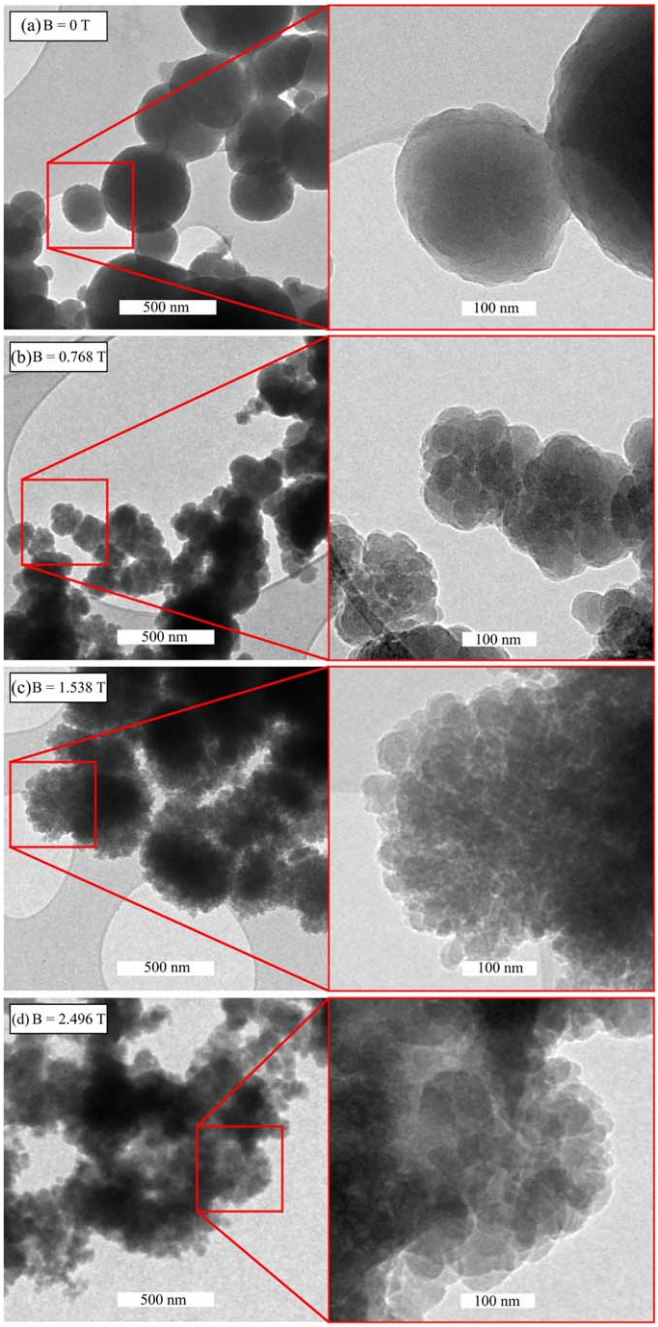

Figure 7. TEM images of dust particles grown for different magnetic fields. The other discharge conditions are the same as in figure 4.

of the substrate, where large amounts of dust particles were collected as well as on the edge of the substrate where a thinner coating was observed (especially at large magnetic fields).

In figure 8, Raman spectra of particles grown at $B = 0$ T, $B = 0.256$ T, $B = 1.024$ T, and $B = 2.496$ T are plotted. Figure 8(a) shows the raw spectra, displaying a huge photoluminescence background and weak vibrational bands. Figure 8(b) shows the vibrational bands after the photoluminescence background has been removed. Two broad peaks are visible in the spectra. The main one is located at 1570–1600 cm^{-1} (G band). In the low energy wing of the G band, the D-band at ~1350 cm^{-1} can be distinguished. These bands are assigned to the stretching modes of sp^2 hybridised carbon atoms and are a signature of aromaticity [53, 55, 58]. Peaks that might correspond to C−O and C=O bonds are also located at 1200 cm^{-1} and in the range 1800–1900 cm^{-1} (not shown) [62]. However, their attribution is unsure since the samples were stored in air prior to analysis and the bands can therefore be due to oxygen contamination. In addition, the pristine glass slides on which the dust particles have been collected also display weak bands located close to 1200 and 1800–2000 cm^{-1}.

Spectroscopic parameters of our samples are reported in table 1. As the bands are broad and overlapped, obtaining the exact values is in general difficult because several fitting models involving two main bands (the G

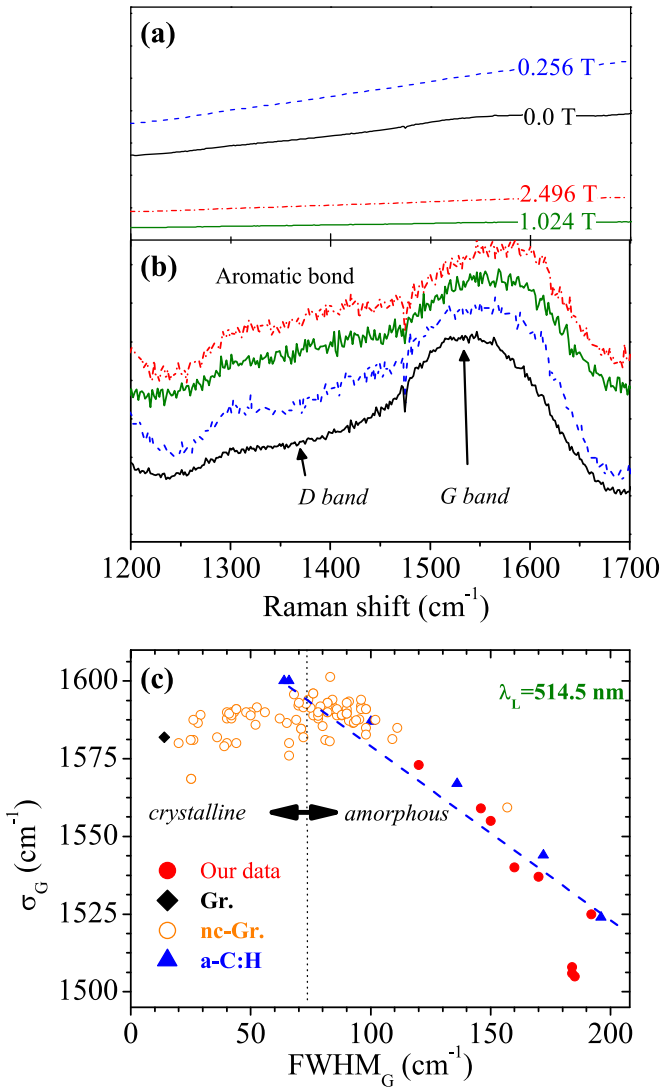

Figure 8. Raman spectra for dust particles grown at $B = 0$ T, $B = 0.256$ T, $B = 1.024$ T, and $B = 2.496$ T. The particles were located at the center of the substrate. (a) Raw spectra. (b) Spectra with linear background (baseline) removed a normalised to the height of the G-band. (c) σ_G as a function of $FWHM_G$ (edge and centre data points). See details in the text for the comparison of the samples.

Table 1. Position, width of the G-band and ratio of the slope of the baseline the spectrum over the intensity of the G-band for dust particles grown at different magnetic fields.

B (T)	σ_G (cm^{-1})		$FWHM_G$ (cm^{-1})		m/I_G (μm)	
	centre	edge	centre	edge	centre	edge
0.0	1540	1537	160	170	89.5	83.5
0.256	1559	1506	146	184	208	37.7
1.024	1555	1505	150	185	104	15.5
2.496	1573	1508	120	184	192	8.4

and D bands) plus additional subbands (up to three extra bands) can be found in the literature. More details on the subject can be found in [63]. In order to avoid any choice of models, we directly took the spectroscopic parameters of spectra of reference samples (graphite, nanocrystalline graphite, nc-Gr. [64], and hydrogenated amorphous carbon, a-C:H [60]) and applied the same procedure to our samples in order to compare them directly to well characterised materials. Figure 8(c) shows the position of the G-band σ_G as a function of its full width at half maximum $FWHM_G$ for all the samples. Reference samples are spread around a curve which

changes its slope around FWHMG $=$ 80–100cm^{-1} which delimits the transition between crystalline and amorphous carbon. From that comparison, we can conclude that our samples are clearly amorphous.

In table 1, σ_G , FWHM$_G$ and, the ratio m/I_G, where m is the slope of the baseline, and I_G is the height of the G-band, are given for dust particles grown different magnetic fields. This ratio can be used to get a very rough estimate of the H-content of carbonaceous materials [65]. For instance, it has been used recently to investigate graphitisation of cabornaceous nanoparticles, and their hydrogen content [66]. A value of $m/I_G \sim 100$ is close to a H content of 50% whereas a value of $m/I_G \sim 10$ is close to a H content of 40 percent.Note that since the data point distribution obtained by Casiraghi *et al* is quite broad [65], m/I_G gives only an estimate. In our case, m/I_G ∼100 for the dust particles indicating a hydrogen content of ∼50% which is the expected value for particles grown in Ar/C_2H_2.

When $B = 0$ T, the Raman spectra recorded at the center and the edges of the sample coincide. It changes when the value of the applied magnetic field value increases. On the edges, m/I_G diminishes by a decade from ∼100 μm to ∼10 μm whereas it remains nearly constant in the centre, varying only from ∼100 μm to 200 μm. A qualitative interpretation is that, when the magnetic field increases, the hydrogen content does not change too much at the centre of the samples (i.e. in the dust particles) whereas it slightly decreases on the edges of the sample (in the coating). The value of FWHM$_G$ at the centre decreases from ∼160 cm^{-1} at $B = 0$ T to ∼120 cm^{-1} at B $= 2.496$ T, while being nearly constant at the edges (∼185 cm^{-1}). A possible interpretation is that the local order in the dust particles is slightly higher for particle growth at high magnetic fields.

The Raman microscopy results support the hypothesis of dust amorphous hydrogenated carbon particles consisting of large numbers of very small aromatic domains. Note that the G band position σ_G, FWHM$_G$, and the D/G band intensity ratio could be used to determine the degree of order of the carbonaceous dust materials [57, 60]. This is however beyond the scope of the present study.

5. Discussion

5.1. Evolution of the pristine argon discharge

To understand the process of particle growth in a magnetised plasma, it is necessary first to understand how a pristine argon discharge is affected by the magnetic field. For this purpose, a basic diffusion model of the plasma has been developed. We first assume a quasi-neutral transport (ambipolar diffusion). We also consider that the plasma is completely surrounded by conducting walls so that the ambipolar field is effectively short circuited at the end of the discharge plasma. The geometry of the system is reduced to a simple cylinder of radius R and length L. The powered electrode is at the top of the cylinder and has a radius $R_a < R$. To explain the behaviour of the discharge at different magnetic fields, a simple diffusion equation is used [25, 67]

$$\frac{\partial n(r,\,z)}{\partial t} = D_{a\perp}\nabla_{\perp}^{2} n(r,\,z) + D_{a\parallel}\frac{\partial^{2} n(r,\,z)}{\partial z^{2}} + \nu_{iz}(r,\,z)n(r,\,z), \tag{1}$$

where $D_{a\parallel}$ is the parallel diffusion coefficient defined as:

$$D_{a\parallel} = \frac{k(T_e + T_i)/e}{\mu_i^{-1} + \mu_e^{-1}}, \tag{2}$$

with $\nu_{iz}(r, z)$ the ionisation frequency, $\mu_{e(i)}$ the electron (ion) mobility coefficients, k the Boltzmann constant, e the elementary charge and, $T_{e(i)}$ the electron (ion) temperature. The perpendicular diffusion coefficient in the framework of the Simon's ambipolar diffusion joint model is [67]:

$$\begin{aligned} D_{a\perp} = {} & \frac{k/e}{(\mu_i^{-1} + \mu_e^{-1})}\left(\frac{(T_e + T_i)}{(1 + \mu_e\mu_i B^2)}\right) \\ & + \frac{k/e}{(\mu_i^{-1} + \mu_e^{-1})}\frac{\mu_e\mu_i B^2}{\frac{T_e/T_i - \mu_i/\mu_e}{1 - (\mu_i/\mu_e)(T_e/T_i))} + \mu_e\mu_i B^2} \\ & \times\left(\frac{T_e}{1 + \mu_e^2 B^2} + \frac{T_i}{1 + \mu_i^2 B^2}\right). \end{aligned} \tag{3}$$

In cc-rf discharges, the ionisation rate is the highest at the sheath below the powered electrode and decreases as a function of the distance from the powered surfaces [68, 69]. However, in the plasma bulk in the interelectrode gap beneath the powered surfaces, the ionisation rate is still reasonably high (2-3 times lower than its maximum value) while it falls rapidly to zero in the region mostly surrounded by grounded surfaces. The electron temperature varies in contrast more slowly [68]. For this reason, the ionisation frequency is approximated as:

$$\nu_{\rm iz}(r,\,z) = \nu_{\rm iz}(r) = \begin{cases} \nu_{\rm iz}, & R \leqslant R_{\rm a}, \\ 0, & R > R_{\rm a}. \end{cases} \tag{4}$$

Ionisation is due to inelastic collision between electron and atoms. For argon, the ionisation frequency can be approximated as [67, 70]:

$$\nu_{\rm iz} = p \cdot 8.13 \cdot 10^8 \left(\frac{kT_{\rm e}}{e}\right)^{0.68} \exp\left(\frac{-\epsilon_{\rm I} e}{kT_{\rm e}}\right), \tag{5}$$

where p is given in Torr and $\epsilon_{\rm I} = 15.76$ eV is the threshold ionisation energy of argon. The solution of the diffusion equation can be easily calculated:

$$n(r,\,z) = \begin{cases} n_0 \cos\left(\pi\frac{z}{L}\right) J_0(\alpha_P r), & R \leqslant R_{\rm a}, \\ n_0 \cos\left(\pi\frac{z}{L}\right) J_0(\alpha_P R_{\rm a}) \frac{K_0(\alpha_G R) I_0(\alpha_G r) - K_0(\alpha_G r) I_0(\alpha_G R))}{K_0(\alpha_G R) I_0(\alpha_G R_{\rm a}) - K_0(\alpha_G R_{\rm a}) I_0(\alpha_G R))}, & R > R_{\rm a}, \end{cases} \tag{6}$$

where J_k, K_k and I_k are the Bessel function of the first kind and the modified Bessel functions of the first and second kind of order k, respectively. The coefficient α_P and α_G define the characteristic length of diffusion and are defined as follows:

$$\alpha_P^2 = \frac{\nu_{\rm iz}}{D_{\rm a\perp}} - \left(\frac{\pi}{L}\right)^2 \frac{D_{\rm a\parallel}}{D_{\rm a\perp}}, \tag{7}$$

$$\alpha_G^2 = \left(\frac{\pi}{L}\right)^2 \frac{D_{\rm a\parallel}}{D_{\rm a\perp}}. \tag{8}$$

At a given pressure and magnetic field, the $\alpha_{P,G}$ coefficients depend only on the electron temperature. The derivative of the plasma density being continuous, the electron temperature can then be found by solving:

$$\left.\frac{\partial n(r,\,z)}{\partial r}\right|_{r=R_{\rm a}^-} = \left.\frac{\partial n(r,\,z)}{\partial r}\right|_{r=R_{\rm a}^+} \tag{9}$$

or

$$\begin{aligned} 0 = {} & \alpha_P J_1(\alpha_P R_{\rm a}) + \alpha_G J_0(\alpha_P R_{\rm a}) \\ & \times \frac{K_0(\alpha_G R) I_1(\alpha_G R_{\rm a}) + I_0(\alpha_G R) K_1(\alpha_G R_{\rm a}))}{K_0(\alpha_G R) I_0(\alpha_G R_{\rm a}) - K_0(\alpha_G R_{\rm a}) I_0(\alpha_G R))}. \end{aligned} \tag{10}$$

equation (10) was solved numerically at $p = 300$ mTorr for different magnetic fields and the resulting density profiles are plotted in figure 9(a). It is shown that with increasing the magnetic field the plasma is increasingly confined under the powered electrode. This is in qualitative agreement with the experimental observation of the glow distribution presented in figure 2. It is also interesting to note that the increase of the magnetic field results in a slight decrease of the electron temperature (figure 9(b)). This is due to a better confinement of the electrons in the glow which leads to a more efficient ionisation of the gas. This can also explain the faster decrease of the gas pressure during the particle growth experiment with an applied magnetic field (figure 4(a)) caused by improved dissociation of acetylene which resulted from better electron confinement. Moreover, the forward RF power was kept constant during the experiment. In our model, by assuming that the effective rf power coupled to the plasma does not change and is totally used to ionise the gas and is then lost by recombination on the walls of the chamber, the relative density of the plasma, $n/\langle n\rangle$ where $\langle n\rangle$ is the plasma density averaged over the volume of the plasma chamber, compared to the case without magnetic field can be calculated[4]. Results are presented in figure 9(a). As can be seen, despite the fact the electron temperature decreases with increasing magnetic field, the relative plasma density increases with the magnetic field, qualitatively explaining the experimental observation of a more intense glow emission at high magnetic field. Note that since our model is not taking into account the spatial dependence of the ionisation rate and the electron temperature nor the surfaces covered by the dielectric glass slide, it is unable to explain the plasma filamentation observed experimentally.

Following the work of Lieberman and Savas [71], the self-bias voltage of the powered electrode can be estimated. In asymmetric cc-rf discharges, the powered and grounded electrode having different areas, the voltage drop in front of the powered (active) electrode $V_{\rm a}$ is different from the voltage drop $V_{\rm g}$. The voltage ratio $(V_{\rm a}/V_{\rm g})$ can be obtained from the current fluxes at each electrode. In Lieberman and Savas model [71], the applied rf voltage is dropped across a thin sheath. It is also assumed that the glow region between the electrodes has a thickness much greater than those of the sheaths so that the discharge is maintained by ion generation in the glow and losses at the electrode. An approximate form of the dc voltage drop $V_{\rm a}$ and the rf voltage amplitude

[4] The plasma density cannot be properly estimated since it is not possible to know exactly how much power is effectively coupled to the plasma.

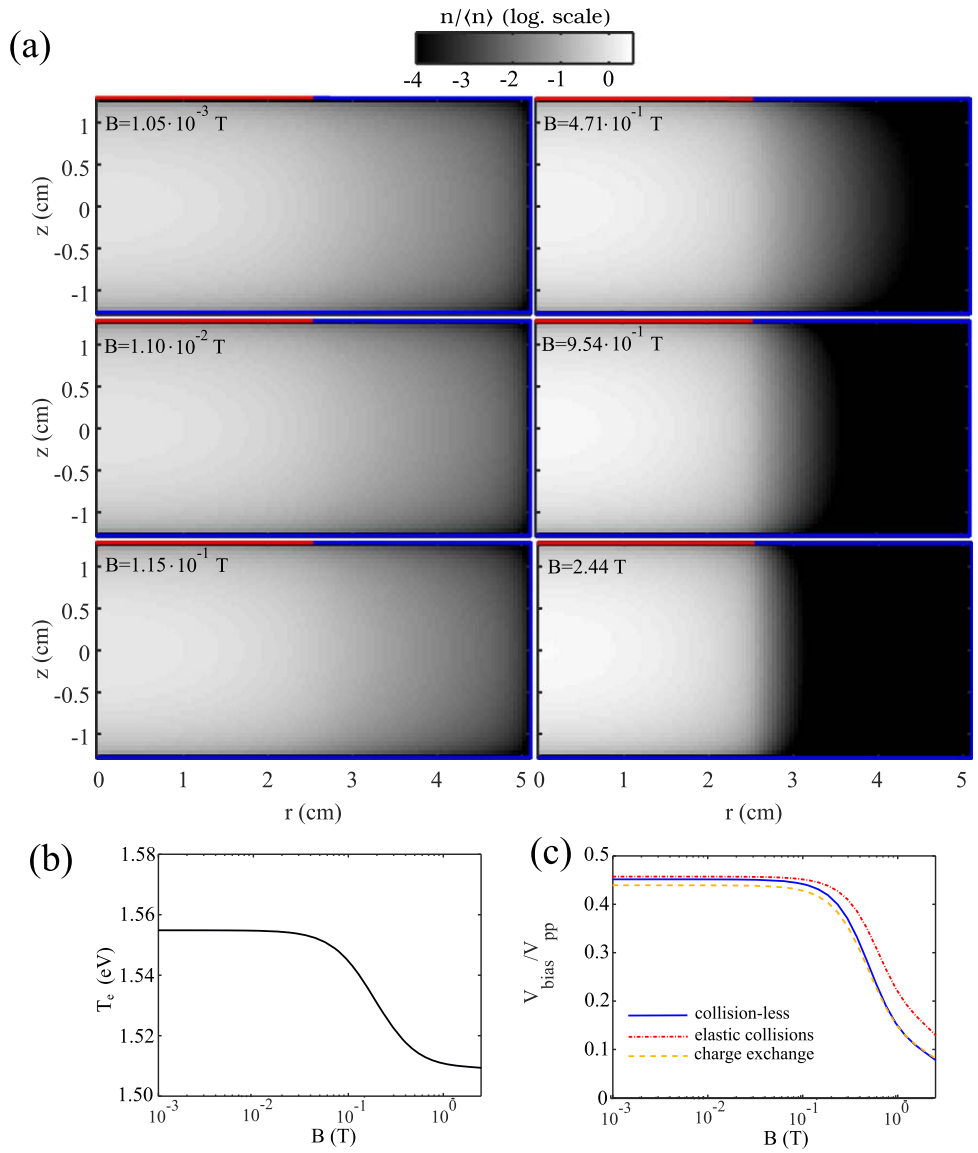

Figure 9. Results of the calculation: (a) plasma density distribution for different magnetic field strengths. The red lines represent the powered electrode and the blue lines represent the grounded surfaces. (b) Electron temperature as a function of the magnetic filed strength. (c) V_{bias}/V_{pp} as a function of magnetic field strength. The argon pressure is $p = 300$ mTorr and the peak-to-peak voltage is $V_{pp} = 300$ V.

$\tilde{V}_a$ is [71]:

$$V_a = (k_b T_e/e)\ln[I_0(\tilde{V}_a/T_e)] + (k_b T_e/e)\ln[m_i/(2\pi m_e)],$$
$$V_a \approx \tilde{V}_a + V_{fa}, \quad \text{if} \quad T_e \ll \tilde{V}_a, \tag{11}$$

where the floating potential V_{fa} is defined as:

$$V_{fa} = (k_b T_e/2e)\ln[m_i T_e/(4\pi^2 m_e \tilde{V}_a)] \tag{12}$$

In the case of high voltage capacitive sheath, $V_{fa} \ll V_a$ and $\tilde{V}_a \approx V_a$ so, by considering capacitive sheath, the rf current current density can be related to the dc sheath voltage:

$$J_a(\boldsymbol{x}) \propto V_a/s_a(\boldsymbol{x}) \tag{13}$$

Depending on the ion-neutral mean free path compared to the sheath thickness s, collisions can play a role and influence the plasma density at the sheath edge n_s [71]. For a collision-less sheath:

$$n_{sa} \propto V_a^{3/2}/s_a(\boldsymbol{x})^2 \tag{14}$$

For a collisional-resonant charge transfer- sheath:

$$n_{sa} \propto V_a^{3/2}/s_a(\boldsymbol{x})^{5/2} \tag{15}$$

For a collisional-elastic scattering- sheath:

$$n_{sa} \propto V_a^2 / s_a(\boldsymbol{x})^3 \tag{16}$$

The rf current flowing through the rf electrode is:

$$I_a \propto \int_{S_a} J_a(\boldsymbol{x}) d^2x \tag{17}$$

A similar expression can be obtained for the current flowing through the grounded surface I_g. By equating the two currents the following scaling formula can be obtained [71]:

$$\frac{V_a}{V_g} = \left\{ \left(1 - \frac{V_{fg}}{V_g}\right)\left(1 - \frac{V_{fa}}{V_a}\right)^{-1} \times \left[\int_{S_g} n_{sg}^p(\boldsymbol{x}) d^2x\right]\left[\int_{S_a} n_{sa}^p(\boldsymbol{x}) d^2x\right]^{-1} \right\}^q \tag{18}$$

where p and q are exponents corresponding to the sheath scaling law (collision-less: $p = 1/2, q = 3$, elastic collisions: $p = 1/3, q = 4$, charge-exchange collisions: $p = 2/5, q = 5/2$) [71]. The dc voltage drops V_a and V_g can be linked to the peak-to-peak rf voltage V_{pp} applied to the discharge [71]:

$$V_a + V_g = V_{fa} + V_{fg} + V_{pp}/2. \tag{19}$$

In the experiment, the self-bias voltage is:

$$V_{bias} \approx V_a - V_g. \tag{20}$$

Using equations (18) and (19), the normalised bias voltage is [71]:

$$\frac{V_{bias}}{V_{pp}} \approx \frac{1}{2} \frac{V_a/V_g - 1}{V_a/V_g + 1 - V_{fa}/V_g - V_{fg}/V_g}. \tag{21}$$

The density at the sheath boundaries can be obtained by specifying that the ion flow velocity at the walls is perpendicular to the wall and has a velocity equal to the Bohm velocity $u_B = \sqrt{k_B T_e / m_i}$. Under these conditions the ion flux at the walls due to ambipolar diffusions is given by evaluating at the sheath edge:

$$n_s u_B = -\left(D_{a\perp} \nabla_\perp n(r, z) + D_{a\parallel} \frac{\partial n(r, z)}{\partial z}\right). \tag{22}$$

Using equation (6), the plasma-sheath edge density at the cylinder side is:

$$n_{s_1}(R, z) = \frac{n_0 J_0(\alpha_G R_a)}{u_B} D_{a\perp} \alpha_G \cos\left(\frac{\pi z}{L}\right) \times \frac{K_0(\alpha_G R) I_1(\alpha_G R) + I_0(\alpha_G R) K_1(\alpha_G R))}{K_0(\alpha_G R) I_0(\alpha_G R_a) - K_0(\alpha_G R_a) I_0(\alpha_G R))}, \tag{23}$$

and at the cylinder top and bottom:

$$n_{s_2}(r, \pm L/2) = \begin{cases} \frac{n_0 D_{a\parallel} \pi}{u_B L} J_0(\alpha_P r), & R \leqslant R_a, \\ \frac{n_0 D_{a\parallel} \pi}{u_B L} J_0(\alpha_P R_a) \frac{K_0(\alpha_G R) I_0(\alpha_G r) - K_0(\alpha_G r) I_0(\alpha_G R))}{K_0(\alpha_G R) I_0(\alpha_G R_a) - K_0(\alpha_G R_a) I_0(\alpha_G R))}, & R > R_a. \end{cases} \tag{24}$$

In the geometry of our experiment, the integrals of equation (18) are:

$$\int_{S_g} n_{sg}^p(\boldsymbol{x}) d^2x = \int_{-L/2}^{+L/2} n_{s_1}^p \cdot 2\pi R dz + 2\int_{R_a}^{R} n_{s_2}^p \cdot 2\pi r dr + \int_0^{R_a} n_{s_2}^p \cdot 2\pi r dr, \tag{25}$$

and

$$\int_{S_a} n_{sa}^p(\boldsymbol{x}) d^2x = \int_0^{R_a} n_{s_2}^p \cdot 2\pi r dr. \tag{26}$$

From equations (18), (25) and (26), it is obvious that the self-bias voltage does not depend on the maximum plasma density n_0 and u_B.

By solving numerically equations (1)–(26), the normalised self-bias voltage could be calculated. The evolution of the normalised self-bias voltage as a function the magnetic field strength is presented in figure 9(c)

for the different sheath models. As can be seen V_{bias}/V_{pp} exhibits a strong drop for magnetic field strength $B \gtrsim 0.1$ T. These results agree relatively well with the experimental observation of figure 3. The observed discrepancies are due to the simplicity of our model. The experimentally observed decrease of V_{bias} for $B \gtrsim 1$ T is however not explained by our basic ambipolar diffusion model. It might be due to a loss of ionisation when both electrons and ions are magnetised and/or to the influence of the dielectric glass slide on the bottom electrode.

5.2. Dust particle confinement and growth

In order to qualitatively explain the growth dynamics of the nanoparticles, it is necessary to understand how dust particle confinement is affected by the presence of the magnetic field. For this purpose, two-dimensional particle-in-cell (PIC) simulations of a simplified model of our discharge (similar to the one described in the previous section) have been performed using the VSIM software from TechX corporation [72]. The bottom and side walls were grounded. The powered electrode located at the top of the chamber is connected to a 13.56 MHz rf voltage source with a peak-to-peak amplitude $V_{pp} = 400$ V enough to maintain the plasma and a constant vertical magnetic field was imposed. In order to simulate the self-bias of the powered electrode, an additional DC bias was also applied to the powered electrode, the value of which was chosen to roughly correspond to the measured value of the self-bias at a given magnetic field for a pristine argon discharge (see figure 3). A small gap of 1 mm between the powered electrode and the grounded wall was included (to avoid diverging field and also match the gap between the grounded guard ring and the electrode in the experiment). A background Ar gas with a pressure of 95 mTorr was filled in the chamber[5]. An initial electron density at $1 \cdot 10^9$ cm^{-3} was seeded to start the simulation. The collisions involved were electron-neutral collisions that lead to ionisation and ohmic heating. The simulations were run for $\gtrsim$215 rf periods until the electron and ion densities have stabilised[6]. Then the plasma potential and ion density were averaged over 40 rf period. Radial and vertical electric fields were obtained from the gradient of the average potential. Note that only the cross sections for ionisation and one excited level of Argon were used in our simulation. Moreover since the simulations are performed at a constant peak-to-peak voltage instead of constant injected power (as in the experiment), the simulated plasma density cannot be directly compared to our experiments. Finally, the area covered by the dielectric glass slide on the grounded bottom electrode was not included in the simulation. Consequently, the simulation results are only qualitative information of the behaviour of the discharge at different magnetic fields.

In figure 10, the PIC results for $B = 0$ T, $B = 0.032$ T, $B = 0.25$ T and, $B = 0.50$ T are presented. As expected, when increasing the magnetic field, the plasma becomes more confined below the powered electrode (figures 10(a), (e), (i), (m)). These results are in qualitative agreement with the results obtained in the previous section from the simple diffusion model, our experimental observation of the plasma light emission (figure 2), and with measurements made in a similar experimental set-up [49]. However the ion density distribution has a slightly more complicated shape than the one inferred from the diffusion model. The potential and electric fields distributions are also greatly influenced by the presence of the magnetic field.

As can be seen, when there is no applied magnetic field (figures 10(b)–(d)), the potential is nearly constant and the vertical and radial electric fields are close to zero over a large volume of the discharge chamber. Only in the vicinity of the grounded walls and the powered electrode does the electric field reaches values of a few tens of V cm^{-1}, enough to confine negatively charged particles in the plasma. For this reason, the cloud of negatively charged nanoparticles extends in most of the interelectrode space as observed in figure 5(a).

At low magnetic field ($B = 0.032$ T, figures 10(e)–(h)), the gradient of the plasma potential is even weaker than without applied magnetic field. This is due to a decrease of the ambipolar field due to the magnetisation of the electrons which are confined in the discharge. This fact can partially explain the faster growth cycles observed experimentally since the dust particles are only very weakly confined in the plasma by the tiny radial electric field.

When further increasing the magnetic field (figures 10(i)–(p)), the radial confinement reappears but the maximum value of the confining electric field is shifted below the interface between the guard ring and the powered electrode. For radius larger than the powered electrode radius ($r > R_a$), the radial electric field rapidly falls to 0 and the plasma density decreases very quickly. This effect is enhanced by the strength of the magnetic field. For these reasons, at high magnetic field, nanoparticles are not confined at $r > R_a$ and are found only in the volume directly below the powered electrode (see figure 5(c)). The increase of the dust radial confinement when ramping up the magnetic field was also observed in experiments in which the dust particles were grown prior to the magnetic field application [49].

[5] A lower pressure than in the experiments was chosen to limit the number of collisions and reduce the computational time. The simulated values of densities, potential and fields are therefore not be directly comparable to the experiments. However the tendencies remain the same and are enough for a qualitative study.

[6] The higher the magnetic field, the longer the equilibration run.

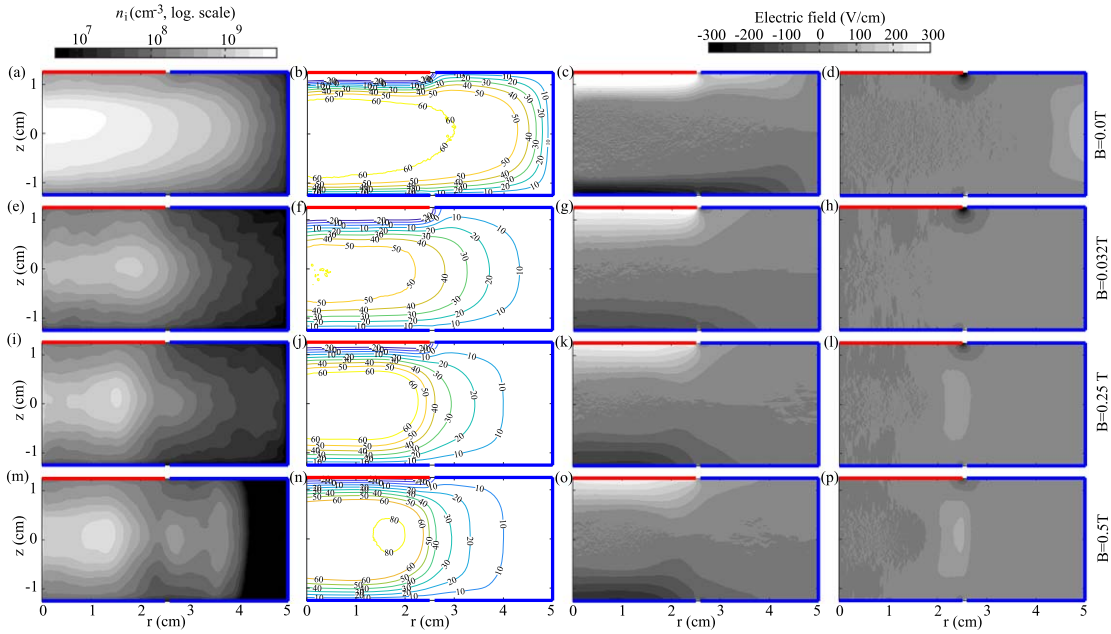

Figure 10. Ion density distribution (a), (e), (i), (m), Potential contour (b), (f), (j), (n), vertical electric field (c), (g), (k), (o), and radial electric field (d), (h), (l), (p) obtained from PIC simulation (pure argon, 1 excited argon neutral level) for $V_{pp} = 400$ V. (a), (b), (c), (d) $B = 0$ T, $V_{bias} = -90$ V, (e), (f), (g), (h) $B = 0.0.032$ T, $V_{bias} = -90$ V, (i), (j), (k), (l) $B = 0.25$ T, $V_{bias} = -50$ V and, (m), (n), (o), (p) $B = 0.50$ T, $V_{bias} = -30$ V The red lines represent the powered electrode and the blue lines represent the grounded surfaces.

From figure 10, it can also be seen that the vertical electric field in the sheath above the grounded electrode (as well as below the powered electrode) seems lower in magnetised discharges than in non-magnetised discharges (at constant power instead of constant V_{pp}, the effect might not be as strong). Moreover, the maximum ion density which is roughly at the centre of the discharge in the non-magnetised plasma (figure 10(a)), is shifted toward the side in the magnetised cases (figures 10(e), (i), (m)). Ion drag force is known to play an important role in the spatial organisation of growing nanoparticle clouds (such as dust 'voids' for instance [46, 73, 74]). The difference in ionisation and the weaker sheath electric fields might be the reason for the localisation of the dust particle cloud close to the bottom electrode for sufficiently high magnetic fields (see figure 5(c)). Note that the presence of the dielectric glass slide is not taken into account in our simulation which certainly influences the electric fields at high magnetic fields. It was indeed reported in section 3.2 that the dust cloud was confined near the glass-metal interface of the multi-part grounded electrode.

In the magnetised discharges, since the growing dust cloud is confined near or in the sheath above the grounded electrode, it can be subject to dust density waves (DDWs) which are spontaneously excited within the sheath when the dust particle density is high enough. DDWs are known to significantly enhance the agglomeration rate between particles by transferring significant kinetic energy to the particles thereby allowing them to overcome Coulomb repulsion [48, 50]. Moreover, the filamentation of the plasma when the magnetic field is high [49, 75] might also be a source of kinetic energy helping agglomeration. Thus the rapid agglomeration observed in the magnetised discharge could be due to the confinement of the growing cloud near the grounded electrode. It was also observed experimentally that the dust particle size distribution was much wider for growth occurring in strongly magnetised plasma ($B > 0.25$T) compared to dust grown in non or slightly magnetised plasma (via laser-light scattering, figure 5(c) and in SEM and TEM pictures, figures 6 and 7). Since in strongly coupled dusty plasmas, agglomeration is enhanced by a dispersed distribution in the sizes of the growing nanoparticles (due to charge fluctuation and the occupation of positively charged states of the smaller nanometre size particles) [76], the agglomeration can be further enhanced. One could argue that the presence of the magnetic field could also directly enhance the agglomeration due to stronger charge fluctuations induced by the reduction of the charging fluxes [77–80]. However, the magnetic field significantly affects the charging fluxes when $\beta_e = \sqrt{(\pi T_e m_e)/2e^2B^2} > 1$ [78]. Assuming $T_e \sim 1.5$eV, the charge of the particle will be strongly affected only when $r_d \gtrsim 3.66/B$ μm. In our experiments, the particles did not reach sizes large enough to have their charges significantly affected. However, the effect can be indirect through modifications of the discharge parameters [67, 81]. The magnetisation of the dust particles (i.e. the dust particle gyroradii become small enough to consider them magnetised [17]) might also play a role in the agglomeration process.

6. Conclusion

In this article, the influence of a constant magnetic field on discharge parameters and particle growth in a capacitively coupled rf discharge has been studied. Experiments were performed in pure argon and argon-acetylene plasmas at magnetic fields up to $B = 2.5$ T. It was found that high magnetic field strength has a major effect on the plasma glow distribution and the self-bias voltage of the powered electrode. To understand the plasma discharge characteristics, a basic ambipolar diffusion model taking into account the diffusion perpendicular and parallel to the magnetic field was developed. The model confirmed that a reduction of the perpendicular diffusion at high magnetic field would have a significant impact on the discharge and qualitatively good agreement was found between the model and the experimental observations of the reduction of the self-bias. Complementary PIC simulations have shown that the electric fields are also affected by the magnetic field.

The magnetic field also had a significant influence on the morphology of nanoparticle that are grown in the plasma. The addition of acetylene to the discharge led to the formation of carbon nanoparticles. At low magnetic fields, $B < 0.1$ T, the well-known cyclic growth behavior was observed with the opening of a void region in the plasma bulk in which the next generation of nanoparticles could grow. At higher magnetic fields, $B > 0.1$ T, no growth cycles were reported. However, a cloud of nanoparticles above the grounded bottom electrode appeared more rapidly than in the low magnetic field cases with larger agglomerates formed above the grounded, bottom electrode in just tens of seconds after plasma ignition. The enhanced agglomeration, which may be the reason of the observation of the big porous spherical agglomerates, could be explained by the presence of dust acoustic waves and plasma filamentation that appear in the plasma at the higher magnetic fields. Electron microscopy, both SEM and TEM, revealed that the big nanoparticles were porous spherical agglomerates of very small nanoparticles. Raman spectroscopy did not reveal any major differences of chemical properties and structural order between particles formed at lower versus higher magnetic fields. In all of the investigated synthesis conditions, the grown dust particles were composed of amorphous carbon.

In future studies, different magnetic field and electrode configurations will be investigated. Complementary diagnostics such as optical emission spectroscopy and light extinction spectrometry [82] will be added in order to obtain more insight on the influence of the magnetic field on dust growth kinetics. A particular interest will be on the influence of plasma filamentation on particle growth.

Acknowledgments

The authors would like to thank Prof M Bradley for his useful remarks and suggestions. This work is supported by funding from the US Dept. of Energy, Grant Number DE- SC0016330, and by the National Science Foundation, Grant Numbers PHY-1613087 and PHY-1126067. Additional support is provided by the NSF EPSCoR program (OIA- 1655280).

ORCID iDs

L Couëdel https://orcid.org/0000-0003-0749-9273
M P Khanal https://orcid.org/0000-0001-8265-4718

References

[1] Bouchoule A 1999 *Dusty Plasmas: Physics, Chemistry and Technological Impacts in Plasma Processing* (New York: Wiley)
[2] Morfill G E and Ivlev A V 2009 *Rev. Mod. Phys.* **81** 1353
[3] Shukla P K and Mamun A A 2002 *Introduction to Dusty Plasma* (Bristol: IOP Publishing)
[4] Morfill G E, Grun E, Goertz C K and Johnson T V 1983 *Icarus* **53** 230–5
[5] Mitchell C J, Horanyi M, Havnes O and Porco C C 2006 *Science* **311** 1587–9
[6] Mann I, Meyer-Vernet N and Czechowski A 2012 *Nanodust in the Solar System: Discoveries and Interpretations* vol 385 (Berlin: Springer)
[7] Cavarroc M, Jouanny M C, Radouane K, Mikikian M and Boufendi L 2006 *J. Appl. Phys.* **99** 064301
[8] Lopez T and Mangolini L 2014 *J. Vac. Sci. Technol.* B **32** 061802
[9] Mikikian M *et al* 2017 *Plasma Phys. Control. Fusion* **59** 014034
[10] Selwyn G S, Singh J and Bennett R S 1989 *J. Vac Sci. Technol.* A **7** 2758
[11] Cabarrocas P R I, Nguyen-Tran T, Djeridane Y, Abramov A, Johnson E and Patriarche G 2007 *J. Phys. D: Appl. Phys.* **40** 2258
[12] Kortshagen U R, Sankaran R M, Pereira R N, Girshick S L, Wu J J and Aydil E S 2016 *Chem. Rev.* **116** 11061
[13] Bouchoule A and Boufendi L 1993 *Plasma Sources Sci. Technol.* **2** 204
[14] Watanabe Y 2006 *J. Phys. D: Appl. Phys.* **39** R329
[15] Woodard A, Shojaei K, Nava G and Mangolini L 2018 *Plasma Sources Sci. Technol.* **27** 104003
[16] Bilik N, Anthony R, Merritt B, Aydil E and Kortshagen U 2015 *J. Phys. D: Appl. Phys.* **48** 105204
[17] Thomas E Jr, Merlino R L and Rosenberg M 2012 *Plasma Phys. Control. Fusion* **54** 124034
[18] Calafat M, Escaich D, Clergereaux R, Raynaud P and Segui Y 2007 *Appl. Phys. Lett.* **91** 181502

[19] Nafarizal N and Sasaki K 2012 *J. Phys. D: Appl. Phys.* **45** 505202
[20] Drenik A, Yuryev P, Vesel A, Margot J and Clergereaux R 2013 *Phys. Plasmas* **20** 100701
[21] Matyash K, Fröhlich M, Kersten H, Thieme G, Schneider R, Hannemann M and Hippler R 2004 *J. Phys. D: Appl. Phys.* **37** 2703
[22] Thomas E *et al* 2014 *J. Plasma Phys.* **80** 803–8
[23] Thomas E, Konopka U, Lynch B, Adams S, LeBlanc S, Merlino R L and Rosenberg M 2015 *Phys. Plasmas* **22** 113708
[24] Raizer Y P, Shneider M N and Yatsenko N A 1995 *Radio-Frequency Capacitive Discharges* ed C P LLC (Florida: CRC Press LLC)
[25] Lieberman M A and Lichtenberg A J 1994 *Principles of Plasma Discharges and Materials Processing* (New York: Wiley) Wiley
[26] Wattieaux G and Boufendi L 2012 *Phys. Plasmas* **19** 033701
[27] Massereau-Guilbaud V, Géraud-Grenier I and Plain A 2009 *J. Appl. Phys.* **106** 113305
[28] Wattieaux G, Carrasco N, Henault M, Boufendi L and Cernogora G 2015 *Plasma Sources Sci. Technol.* **24** 015028
[29] Wattieaux G, Mezeghrane A and Boufendi L 2011 *Phys. Plasmas* **18** 093701
[30] Hundt M, Sadler P, Levchenko I, Wolter M, Kersten H and Ostrikov K K 2011 *J. Appl. Phys.* **109** 123305
[31] Deschenaux C, Affolter A, Magni D, Hollenstein C and Fayet P 1999 *J. Phys. D: Appl. Phys.* **32** 1876
[32] Stoykov S, Eggs C and Kortshagen U 2001 *J. Phys. D: Appl. Phys.* **34** 2160
[33] Herrebout D, Bogaerts A, Gijbels R, Goedheer W J and Vanhulsel A 2003 *IEEE Trans. Plasma Sci.* **31** 659
[34] Baby A, Mahony C M O and Maguire P D 2011 *Plasma Sources Sci. Technol.* **20** 015003
[35] Winter J, Berndt J, Hong S H, Kovačević E, Stefanović I and Stepanović O 2009 *Plasma Sources Sci. Technol.* **18** 034010
[36] Cavarroc M, Mikikian M, Tessier Y and Boufendi L 2008 *Phys. Rev. Lett.* **100** 045001
[37] Couëdel L, Mikikian M, Samarian A A and Boufendi L 2010 *Phys. Plasmas* **17** 083705
[38] Heidemann R J *et al* 2011 *Phys. Plasmas* **18** 053701
[39] Killer C, Himpel M and Melzer A 2014 *Rev. Sci. Instrum.* **85** 103711
[40] Mikikian M, Boufendi L, Bouchoule A, Thomas H M, Morfill G E, Nefedov A P, Fortov V E and the PKE-Nefedov team 2003 *New J. Phys.* **5** 19.1
[41] Mikikian M, Cavarroc M, Couëdel L and Boufendi L 2006 *Phys. Plasmas* **13** 092103
[42] Mikikian M, Couëdel L, Cavarroc M, Tessier Y and Boufendi L 2007 *New J. Phys.* **9** 268
[43] Pilch I and Greiner F 2017 *J. Appl. Phys.* **121** 113302
[44] Praburam G and Goree J 1996 *Phys. Plasmas* **3** 1212
[45] Samsonov D and Goree J 1999 *J. Vac Sci. Technol.* A **17** 2835
[46] Samsonov D and Goree J 1999 *Phys. Rev.* E **59** 1047
[47] Greiner F, Carstensen J, Köhler N, Pilch I, Ketelsen H, Knist S and Piel A 2012 *Plasma Sources Sci. Technol.* **21** 065005
[48] Dap S, Hugon R, Lacroix D, de Poucques L, Briancon J-L and Bougdira J 2013 *Phys. Plasmas* **20** 033703
[49] Tadsen B, Greiner F and Piel A 2014 *Phys. Plasmas* **21** 103704
[50] Du C-R, Thomas H M, Ivlev A V, Konopka U and Morfill G E 2010 *Phys. Plasmas* **17** 113710
[51] Berndt J, Hong S, Kovačević E, Stefanović I and Winter J 2003 *Vacuum* **71** 377
[52] Stefanovic I, Kovacevic E, Berndt J, Pendleton Y and Winter J 2005 *Plasma Phys. Control. Fus.* **47** A179
[53] Tuinstra F and Koenig J L 1970 *J. Chem. Phys.* **53** 1126
[54] Mitura S, Mitura A, Niedzielski P and Chaos P C 1999 *Solitons & Fractals* **10** 2165
[55] Ferrari A C and Robertson J 2004 *Philos. Trans. Royal Soc.* A **362** 2477
[56] Géraud-Grenier I, Massereau-Guilbaud V and Plain A 2004 *Surf. Coat. Technol.* **187** 336
[57] Sadezky A, Muckenhuber H, Grothe H, Niessner R and Pöschl U 2005 *Carbon* **43** 1731
[58] Arnas C, Pardanaud C, Martin C, Roubin P, Temmerman G D and Counsell G 2010 *J. Nucl. Mater.* **401** 130
[59] Wang S M, Pei Y H, Wang X, Wang H, Meng Q N, Tian H W, Zheng X L, Zheng W T and Liu Y C 2010 *J. Phys. D: Appl. Phys.* **43** 455402
[60] Pardanaud C, Martin C, Roubin P, Giacometti G, Hopf C, Schwarz-Selinger T and Jacob W 2013 *Diam. Relat. Mater.* **34** 100
[61] Makdessi G A, Glad X, Dap S, Rojo M, Clergereaux R and Margot J 2017 *J. Phys. D: Appl. Phys.* **50** 155203
[62] Socrates G 2001 *Infrared and Raman Characteristic Group Frequencies: tables and Charts* ed T edition (New York: Wiley)
[63] Merlen A, Buijnsters J and Pardanaud C 2017 *Coatings* **7** 153
[64] Pardanaud C, Martin C and Roubin P 2014 *Vib. Spectrosc.* **70** 187
[65] Casiraghi C, Ferrari A C and Robertson J 2005 *Phys. Rev.* B **72** 085401
[66] Woodard A, Shojaei K, Nava G and Mangolini L 2018 *Plasma Chem. Plasma Process.* **38** 683
[67] Vidal F, Johnston T W, Margot J, Chaker M and Pauna O 1999 *IEEE Trans. Plasma Sci.* **27** 727
[68] Boeuf J P and Pitchford L C 1995 *Phys. Rev.* E **51** 1376
[69] Thomas H M *et al* 2008 *New J. Phys.* **10** 033036 (14pp)
[70] Ashida S, Lee C and Lieberman M A 1995 *J. Vac Sci. Technol.* A **13** 2498
[71] Lieberman M A and Savas S E 1990 *J. Vac Sci. Technol.* A **8** 1632
[72] Nieter C and Cary J R 2004 *J. Comput. Phys.* **196** 448
[73] Morfill G and Tsytovich V N 2000 *Plasma Physics Reports* **26** 682
[74] Akdim M R and Goedheer W J 2001 *Phys. Rev.* E **65** 015401
[75] Thomas E, Konopka U, Merlino R L and Rosenberg M 2016 *Phys. Plasmas* **23** 055701
[76] Annaratone B M, Elskens Y, Arnas C, Antonova T, Thomas H M and Morfill G E 2009 *New J. Phys.* **11** 103013
[77] Tsytovich V N, Sato N and Morfill G E 2003 *New J. Phys.* **5** 43
[78] Patacchini L, Hutchinson I H and Lapenta G 2007 *Phys. Plasmas* **14** 062111
[79] Hutchinson I H and Patacchini L 2010 *Plasma Phys. Control. Fusion* **52** 124005
[80] Lange D 2016 *J. Plasma Phys.* **82** 905820101
[81] Sternberg N, Godyak V and Hoffman D 2006 *Phys. Plasmas* **13** 063511
[82] Barbosa S, Couëdel L, Arnas C, Kumar K K, Pardanaud C and Onofri F R A 2016 *J. Phys. D: Appl. Phys.* **49** 045203